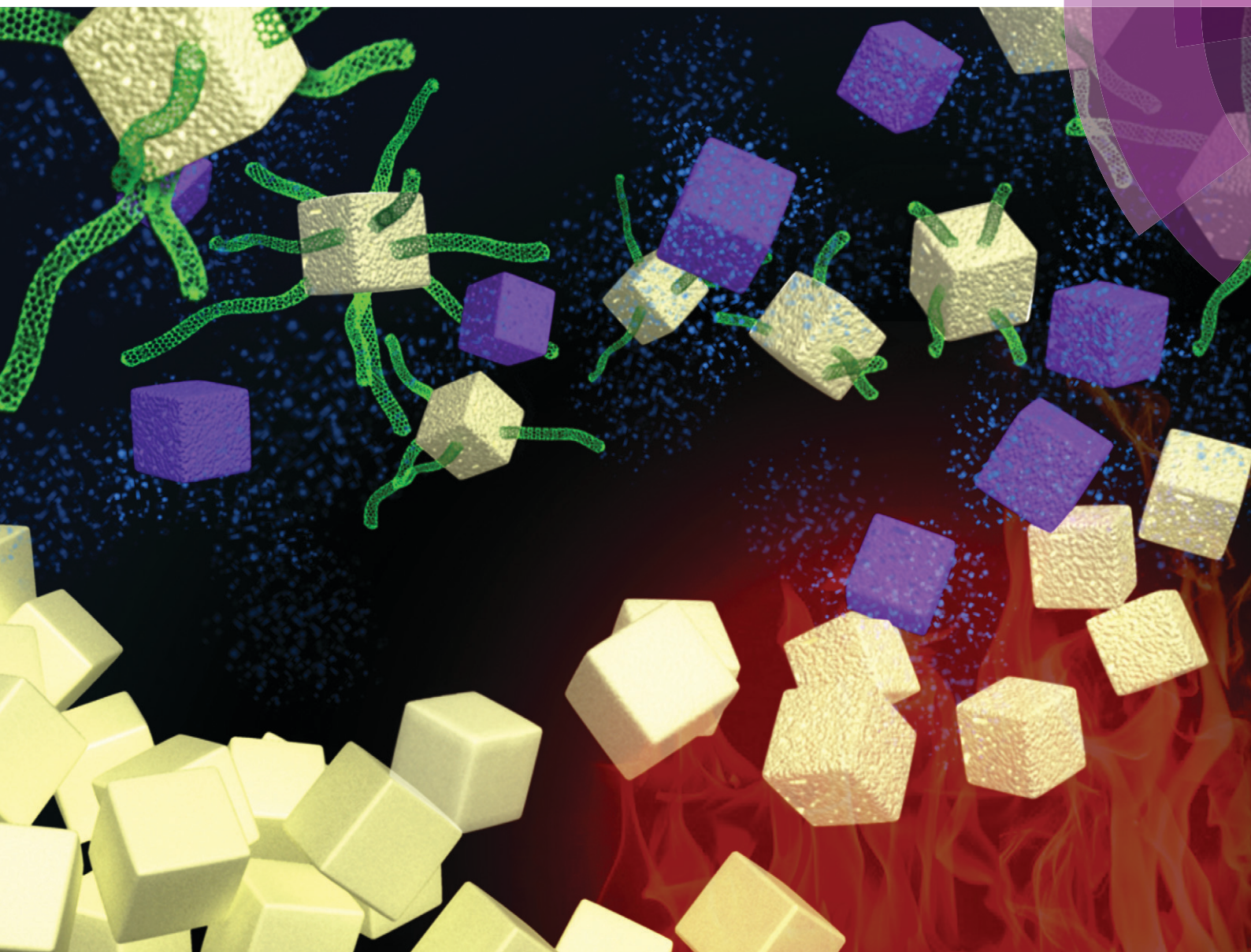


# CrystEngComm

[www.rsc.org/crystengcomm](http://www.rsc.org/crystengcomm)



**COVER ARTICLE**

Zhu, Zhang *et al.*

Flux and surfactant directed facile thermal conversion synthesis of hierarchical porous MgO for efficient adsorption and catalytic growth of carbon nanotubes

Cite this: *CrystEngComm*, 2014, 16, 308

# Flux and surfactant directed facile thermal conversion synthesis of hierarchical porous MgO for efficient adsorption and catalytic growth of carbon nanotubes†

 Wancheng Zhu,<sup>\*a</sup> Linlin Zhang,<sup>a</sup> Gui-Li Tian,<sup>b</sup> Ruguo Wang,<sup>a</sup> Heng Zhang,<sup>a</sup> Xianglan Piao<sup>b</sup> and Qiang Zhang<sup>\*b</sup>

Three-dimensional (3D) hierarchical porous structures have attracted extensive attention owing to their versatile applications. Herein, 3D hierarchical porous MgO superstructures with a well faceted profile and high crystallinity were successfully obtained *via* a facile flux and surfactant directed decomposition of metal oxalates. As a nonionic surfactant, NP-9 served as the dispersing agent and prevented the porous MgO particles from aggregating with each other. The flux NaCl induced vapor migration through the porous structure, favoring the *in situ* crystallization of MgO after the phase conversion from the oxalate precursor, enhancing the toughness of the backbone and further realizing the preservation of the polyhedron-like morphology. The as-obtained hierarchical porous MgO superstructures were very efficient and effective as adsorbents for methylene blue (MB) and a catalyst support for single-walled carbon nanotube (SWCNTs) growth. The as-obtained SWCNTs afford an ultrahigh surface area of 1232 m<sup>2</sup> g<sup>-1</sup>. Such superstructures could be employed as great potential candidates in dye-containing water treatment as well as heterogeneous catalysis.

 Received 16th July 2013,  
Accepted 30th September 2013

DOI: 10.1039/c3ce41394b

[www.rsc.org/crystengcomm](http://www.rsc.org/crystengcomm)

## 1. Introduction

Three-dimensional (3D) hierarchical architectures or superstructures have attracted extensive attention in academia as well as industrial domains owing to the synergistic effect of their nanometer-sized building blocks and overall micrometer-sized structure, which can provide not only a characteristic small size effect but desirable mechanical strength, facile transportation and easy recovery.<sup>1</sup> The hierarchical structures are ubiquitously expected to be promising candidates in fabricating high performance energy conversion and storage devices, catalysts, nanocomposites, and adsorbents, *etc.*<sup>2,3</sup> Metal oxide nanostructures with tunable coordination of the metal cation and oxygen anion as well as a hierarchical porous structure provide them with controllable catalytic activity and semiconductive properties for broad applications in the areas of heterogeneous catalysis, ceramics, electronics, paints and plastics, *etc.*

Among the varieties of oxides, magnesium oxide (MgO) has been known as a traditional refractory material, ceramic and superconducting composite reinforcements, optical transmitters, a novel catalyst carrier for CNT/graphene growth,<sup>4</sup> biodiesel synthesis,<sup>5</sup> and even constituents of CNTs-based composites for supercapacitors,<sup>6</sup> *etc.* Typically, a high temperature (750–1200 °C) based thermal evaporation or chemical vapor deposition (CVD) method was employed to directly prepare monomorph low dimensional MgO nanostructures, including nanorods,<sup>7</sup> nanotubes and the like,<sup>8</sup> as well as hierarchical nanostructures containing 4-fold symmetric nanorod arrays,<sup>9</sup> orthogonal branches<sup>10</sup> or bundles of nanowires.<sup>11</sup> In contrast, mild thermal decomposition of unstable precursors pre-prepared *via* wet-chemistry based methods has emerged as a booming and dominant technique for anhydrous compounds or oxides owing to the relatively low temperature and feasibility of the process. For instance, Mg<sub>2</sub>B<sub>2</sub>O<sub>5</sub> nanowhiskers have been generated from MgBO<sub>2</sub>(OH) nanowhiskers,<sup>12</sup> TiO<sub>2</sub>, Al<sub>2</sub>O<sub>3</sub>, SiO<sub>2</sub> microtubes have been acquired from recyclable MgCO<sub>3</sub>·3H<sub>2</sub>O templates,<sup>13</sup> single crystalline Mn<sub>3</sub>O<sub>4</sub> nanowires were obtained *via* a NaCl and NP-9 assisted thermal conversion of the MnCO<sub>3</sub> precursor.<sup>14</sup> CuO nanowires were fabricated from the calcination of the previously formed copper oxalate nanowires assisted by an ionic-liquid.<sup>15</sup> Similarly, MgO

<sup>a</sup> Department of Chemical Engineering, Qufu Normal University, Shandong, 273165, China. E-mail: zhuwancheng@tsinghua.org.cn; Tel: +86 537 4453130

<sup>b</sup> Department of Chemical Engineering, Tsinghua University, Beijing 100084, China. E-mail: zhang-qiang@mails.tsinghua.edu.cn

† Electronic supplementary information (ESI) available. See DOI: 10.1039/c3ce41394b

nanorods were prepared by thermal dehydration of the rod-like  $\text{Mg}(\text{OH})_2$  nanocrystallites (360 °C),<sup>16</sup> MgO porous nanorods were prepared by calcining hydrated basic magnesium carbonates (450–800 °C),<sup>17</sup> MgO porous nanowires were synthesized by a thermal transformation of hydrated magnesium carbonate hydroxide nanowires (400 °C),<sup>18</sup> MgO porous nanoplates were obtained by a simple hydrothermal treatment of commercial bulk MgO powders followed by mild dehydration (450 °C)<sup>19</sup> or even a single-step  $\text{Mg}(\text{NO}_3)_2$  solution calcination route (500 °C).<sup>20</sup> These nanostructures offer impressive morphologies but when they are used for certain applications, how to manipulate them into anticipated hierarchical nanostructures is still a great challenge.

Most recently, using low dimensional building blocks to build 3D assembled hierarchical bulk nanostructures is highly topical. Impressively, MgO particles with stacks of plates were synthesized by decomposition of the magnesium oxalate dihydrate precursor, which was pre-prepared by mixing magnesium oxochloride gel and ammonium oxalate solution.<sup>21</sup> In addition, micro-sized flower-like MgO nanostructures derived from magnesium glycolate<sup>22</sup> or various morphology MgO architectures originating from magnesium carbonate hydrates<sup>23</sup> as solid base catalysts for Claisen–Schmidt condensation reaction, mesoporous MgO microspheres showing an enhanced adsorption performance for phosphate from aqueous solutions,<sup>24</sup> flower-like and nest-like micro-/nanostructured MgO as adsorbents for As(III) and As(V) removal,<sup>25</sup> and flower-like MgO exhibiting superb adsorption properties for Pb(II) and Cd(II)<sup>26</sup> have also been successfully fabricated. However, the precursors for the reported 3D hierarchical porous MgO superstructures were dominantly formed through weak interaction based self-assembly either by surfactant aided precipitation,<sup>24</sup> oil bath,<sup>25</sup> hydrothermal,<sup>23</sup> or EG mediated<sup>22</sup> and even microwave assisted<sup>26</sup> solvothermal processes. The potential relatively unsatisfactory crystallinity, mechanical properties and morphology stability of the calcined MgO architectures might limit the further practical applications in reality. The templates can be employed to cast 3D nanostructures, however, such replicas were easily lost during calcination. It is still a great challenge to acquire high crystallinity porous metal oxides with robust hierarchical morphology and mechanical properties *via* a facile precursor based synthetic route.

In this contribution, we report a facile flux and surfactant directed mild decomposition of organic precursors for high crystallinity hierarchical nanostructures. Magnesium oxalate was selected as the precursor for the reason that oxalates can be readily synthesized by room temperature coprecipitation, and their decomposition is mild and also free of  $\text{NO}_x$  or  $\text{SO}_x$ . The nonionic surfactant NP-9 with good rinseability has been used in multitudes of applications, serving as the dispersing agent, and NaCl was employed as the flux. It was the successive and synergistic effect of NP-9 and NaCl that promoted the final formation of the hierarchical porous MgO superstructures, which were confirmed as efficient adsorbents for the removal of methylene blue (MB) from mimetic

dye-containing waste water, and also as the catalyst support for single-walled carbon nanotube (SWCNTs) growth.

## 2. Experimental

### 2.1 Preparation of the $\text{MgC}_2\text{O}_4 \cdot 2\text{H}_2\text{O}$ polyhedrons

All reagents were of analytical grade and used as received. The precursor  $\text{MgC}_2\text{O}_4 \cdot 2\text{H}_2\text{O}$  polyhedrons were prepared first *via* a room temperature coprecipitation of sodium oxalate ( $\text{Na}_2\text{C}_2\text{O}_4$ ) and magnesium chloride hexahydrate ( $\text{MgCl}_2 \cdot 6\text{H}_2\text{O}$ ). In a typical procedure, 30 mmol of  $\text{MgCl}_2$  and 30 mmol of  $\text{Na}_2\text{C}_2\text{O}_4$  were dissolved into 30.0 and 170.0 mL of deionized (DI) water, respectively. Then, the  $\text{MgCl}_2$  solution was introduced into the  $\text{Na}_2\text{C}_2\text{O}_4$  solution under vigorous magnetic stirring. After 10 min, the mixture became turbid and was kept stirring for 0.5 h. With subsequent aging for 1.5 h at room temperature, the resultant white slurry was filtered, washed with DI water and absolute ethanol three times, respectively, and finally dried at 70 °C for 6.0 h.

### 2.2 Formation of the hierarchical porous MgO superstructures

In a typical synthesis, 0.01 mol of the pre-prepared  $\text{MgC}_2\text{O}_4 \cdot 2\text{H}_2\text{O}$  powders were mixed with 0.03 mol of NaCl in an agate mortar, ground for 5.0 min first and then for another 0.5 h after the introduction of 8.0 ml of the nonionic surfactant nonylphenol polyoxyethylene ether (NP-9). After that, the mixture was transferred into two porcelain boats which were subsequently located in a horizontal quartz tube furnace, heated to 650 °C (heating rate: 10 °C  $\text{min}^{-1}$ ) and kept in an isothermal state for 2.0 h. After the thermal conversion, the samples were cooled down to room temperature naturally within the tube furnace, then collected and washed with DI water and absolute ethanol three times and finally filtered and dried at 70 °C for 6.0 h. To investigate the effect of the calcination temperature and heating rate on the product, the temperature and heating rate were tuned within 400–800 °C and 2–10 °C  $\text{min}^{-1}$ , respectively, with other conditions unchanged. To better understand the specific effect of NaCl and NP-9, the calcination of the precursor only in the presence of NaCl or NP-9, as well as the thermal decomposition of NP-9 were individually carried out at 250–800 °C within the tube furnace in an air atmosphere.

### 2.3 Hierarchical MgO superstructures as the adsorbents for MB

In a typical process, 30 mg of the as-prepared MgO was added to 20 mL of a MB solution (10 mg  $\text{L}^{-1}$  or 100 mg  $\text{L}^{-1}$ ) under vigorous stirring at room temperature and within a black box to avoid the interference of sunlight. After having been kept stirring for 5–120 min, the above system was filtered and the filtrate was acquired for further characterization. To evaluate the adsorption effect of MgO, digital pictures of the filtrate with different adsorption times were taken, followed by the prompt absorbency measurement of

the filtrate at the optimum wavelength so as to calculate the degradation rate. The degradation rate was calculated *via* eqn (1):<sup>27</sup>

$$A = [(A_0 - A_1)/A_0] \times 100\% \quad (1)$$

where  $A$  is the absorbency,  $A_0$  and  $A_1$  are the absorbency before and after adsorption, respectively.

In order to obtain adsorption isotherms, the MgO superstructures were added to MB solutions with a concentration range from 10 to 800 mg L<sup>-1</sup>. The adsorption was carried out under magnetic stirring for 2.0 h at room temperature with the other conditions kept the same.

The equilibrium adsorption capacity ( $q_e$ ) was calculated according to eqn (2):<sup>24</sup>

$$q_e = \frac{(C_0 - C_e)V}{m} \quad (2)$$

where  $C_0$  and  $C_e$  represent the concentration of the solution before and after adsorption,  $V$  and  $m$  are the volume of the adsorption solution and the mass of the adsorbents, respectively.

#### 2.4 Hierarchical MgO superstructures as the catalyst supports for SWCNTs growth

The MgO based catalyst for CNTs growth was prepared by a facile impregnation method. The hierarchical MgO powder was suspended in distilled water to form a uniform suspension. The Fe(NO<sub>3</sub>)<sub>3</sub>·9H<sub>2</sub>O was dissolved in DI water for a concentration of 0.1 mol L<sup>-1</sup>. Then, the iron containing solution was slowly added dropwise to the suspension. The molar ratio of the salt in the solution to the MgO was controlled by tuning the amount of the solution added to the MgO suspension. The solution was heated to and kept at 100 °C for 12 h, then cooled down to room temperature naturally. After filtration and grinding, the Fe/MgO catalyst for CNTs growth was available with Fe amounts of 0.5 wt%. To synthesize SWCNTs, approximately 2.0 g of the catalyst was sprayed uniformly into a quartz boat, which was then inserted into the center of a quartz tube (diameter: 25 mm, length: 600 mm). The quartz tube, mounted in an electrical tube furnace, was heated to 900 °C (heating rate: 10 °C min<sup>-1</sup>) in an Ar atmosphere. Subsequently, a mixture of CH<sub>4</sub>/Ar (100/300 mL min<sup>-1</sup>) was introduced into the quartz tube and maintained at the reaction temperature for 2.0 min before the furnace was cooled down to room temperature under Ar protection. The products were collected for further morphology and structure analysis. The high purity SWCNTs were obtained by HCl washing and subsequent filtration.

#### 2.5 Characterization

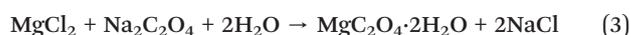
The composition and structure of the samples were identified by X-ray powder diffraction (XRD, D8-Advance, Bruker, Germany), using Cu-K<sub>α</sub> radiation ( $\lambda = 1.54178 \text{ \AA}$ ), a fixed power source (40.0 kV, 40.0 mA) and an aligned silicon detector.

The morphology and microstructure of the samples were examined by high resolution transmission electron microscopy (TEM, JEM-2010, JEOL, Japan) and field emission scanning electron microscopy (SEM, JSM 7401F, JEOL, Japan). The thermal decomposition properties of the precursor was detected by a thermal gravimetric analyzer (TGA, Netzsch STA 409C, Germany), carried out in dynamic air with a heating rate of 10 °C min<sup>-1</sup>. The N<sub>2</sub> adsorption–desorption isotherms were measured at 77 K using a Chemisorption–Physisorption Analyzer (Autosorb-1-C, Quantachrome, USA). The specific surface area was calculated from the adsorption branches in the relative pressure range of 0.05–0.25 using the multipoint Brunauer–Emmett–Teller (BET) method, the pore size distribution was evaluated from the N<sub>2</sub> desorption isotherm using the Barrett–Joyner–Halenda (BJH) method, and the total pore volume was calculated for pores with diameters less than a specific value of  $P/P_0$  *ca.* 0.9956. The pore size distribution of the hierarchical porous MgO superstructures was further evaluated *via* mercury porosimetry.

### 3. Results and discussion

#### 3.1 Preparation of the precursor MgC<sub>2</sub>O<sub>4</sub>·2H<sub>2</sub>O polyhedrons

The chemical composition, morphology and pyrolysis performance of the precursor obtained *via* room temperature coprecipitation for 1.5 h are shown in Fig. 1. As shown in Fig. 1(a), all the diffraction peaks could be indexed to the pure phase of monoclinic glushinskite MgC<sub>2</sub>O<sub>4</sub>·2H<sub>2</sub>O (JCPDS no. 28-0625), similar to the magnesium oxalate dihydrate precursor for the MgO particles with stacks of plates.<sup>21</sup> The chemical reaction involved in this process could be written as follows:



The as-obtained precursor, MgC<sub>2</sub>O<sub>4</sub>·2H<sub>2</sub>O, exhibited an irregular polyhedron-like morphology (Fig. 1(b–c)), with distinct borders and sometimes even small nanoparticles (NPs) attached onto the surfaces. The thermal decomposition properties of the precursor were recorded, as shown by the thermogravimetric-differential scanning calorimetry (TG-DSC) curves in Fig. 1(d). The sample mass decreased gradually at a slow rate below 120 °C due to the elimination of the absorbed water, decreased at a much faster rate at 120–230 °C, then sharply dropped between 410 and 500 °C, and finally remained almost constant thereafter. The mass of the sample decreased from 98.87 to 75.12% at 120–230 °C, indicating *ca.* 23.75% drop of the mass. This was quite similar to the theoretical value (24.32%) for the dehydration of MgC<sub>2</sub>O<sub>4</sub>·2H<sub>2</sub>O to release two moles of crystal water, as shown in eqn (4):



With the increase in the temperature from 410 to 500 °C, the sample exhibited a significant mass drop of 44.94%,

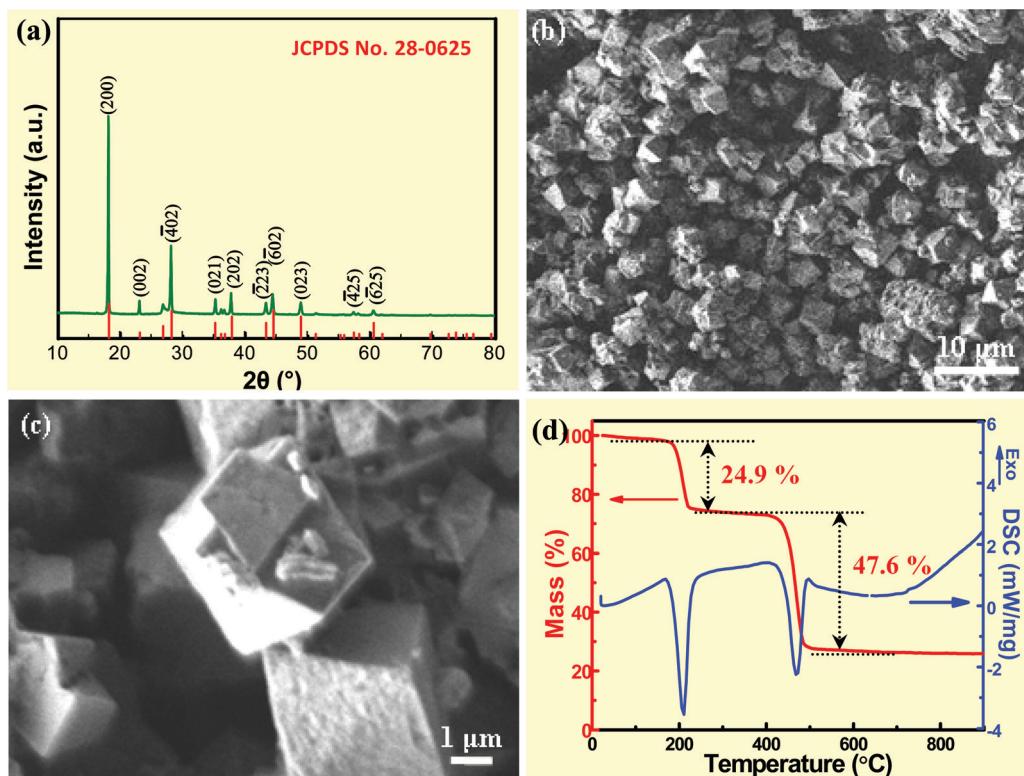
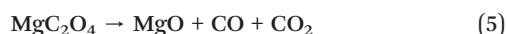


Fig. 1 (a) XRD pattern, (b–c) SEM images, and (d) TG–DSC curves of the precursor  $\text{MgC}_2\text{O}_4 \cdot 2\text{H}_2\text{O}$  (JCPDS no. 28-0625), derived from room temperature coprecipitation of  $\text{MgCl}_2 \cdot 6\text{H}_2\text{O}$  and  $\text{Na}_2\text{C}_2\text{O}_4$  solutions after aging for 1.5 h.

analogous to the theoretical value (48.64%) for the decomposition of  $\text{MgC}_2\text{O}_4$ , indicated by eqn (5):



Corresponding to the change of the sample mass with the temperature, the simultaneously recorded DSC curve demonstrated two remarkable endothermic peaks at 180–230 °C and 425–500 °C, ascribed to the decomposition of the precursor within the two temperature ranges shown as eqn (4) and (5), respectively.

### 3.2 Thermal conversion of the precursor to the hierarchical porous MgO superstructures

Enlightened by the thermal decomposition property of the precursor, to acquire MgO superstructures with high crystallinity and also a well retained polyhedron-like morphology, the pre-prepared  $\text{MgC}_2\text{O}_4 \cdot 2\text{H}_2\text{O}$  polyhedrons were calcined at a relatively high temperature of 650 °C (rather than the generally used 500 °C<sup>28</sup>) for 2.0 h in the presence of NaCl and NP-9. The XRD pattern (Fig. 2(a)) of the calcined product showed that each diffraction peak could be readily indexed to that of the pure phase of periclase MgO (JCPDS no. 45-0946), reconfirming the thermal conversion of the precursor  $\text{MgC}_2\text{O}_4 \cdot 2\text{H}_2\text{O}$  to the final MgO, as shown in the eqn (4) and (5). The SEM image (Fig. 2(b)) demonstrated that the calcined product particles bore a well faceted profile, relatively distinct

edges but rough surfaces. Obviously, the polyhedron-like morphology of the precursors was fairly well preserved with the assistance of NaCl and NP-9, similar to the MgO particles with stacks of plates morphology derived from the dehydration of magnesium oxalate dihydrate at a lower temperature of 500 °C.<sup>21</sup> A higher resolution SEM image (Fig. 2(c)) clearly revealed the as-obtained MgO with hierarchical porous superstructures, containing multitudes of pores with diameters < 200 nm. A typical TEM image (Fig. 2(d)) again indicated that the as-obtained MgO superstructures retained the morphology of the precursor, containing tiny NPs within the body. It was notable that the discrete fine NPs within the TEM image mainly originated from the ultrasonic treatment during the TEM sample preparation. The typical SAED pattern (Fig. 2(d<sub>1</sub>)) corresponding to the selected group of tiny NPs (as shown in the red short dashed line rectangular region) adhered to the bulk MgO superstructure indicated the fine MgO NPs of a distinct crystalline phase, in good agreement with the XRD result (Fig. 2(a)). The interplanar spacing of 0.22 nm detected from the legible lattice fringes (Fig. 2(e)) was quite similar to the standard value for the (200) planes of periclase MgO, reconfirming the high crystallinity of the calcined product. As a matter of fact, the strong diffraction peaks of the XRD pattern, well faceted profile, SAED pattern and high resolution TEM images revealed the as-obtained product had higher crystallinity and predictable better mechanical properties compared with hierarchical porous MgO architectures self-assembled by weak interactions.<sup>12,23–28</sup>

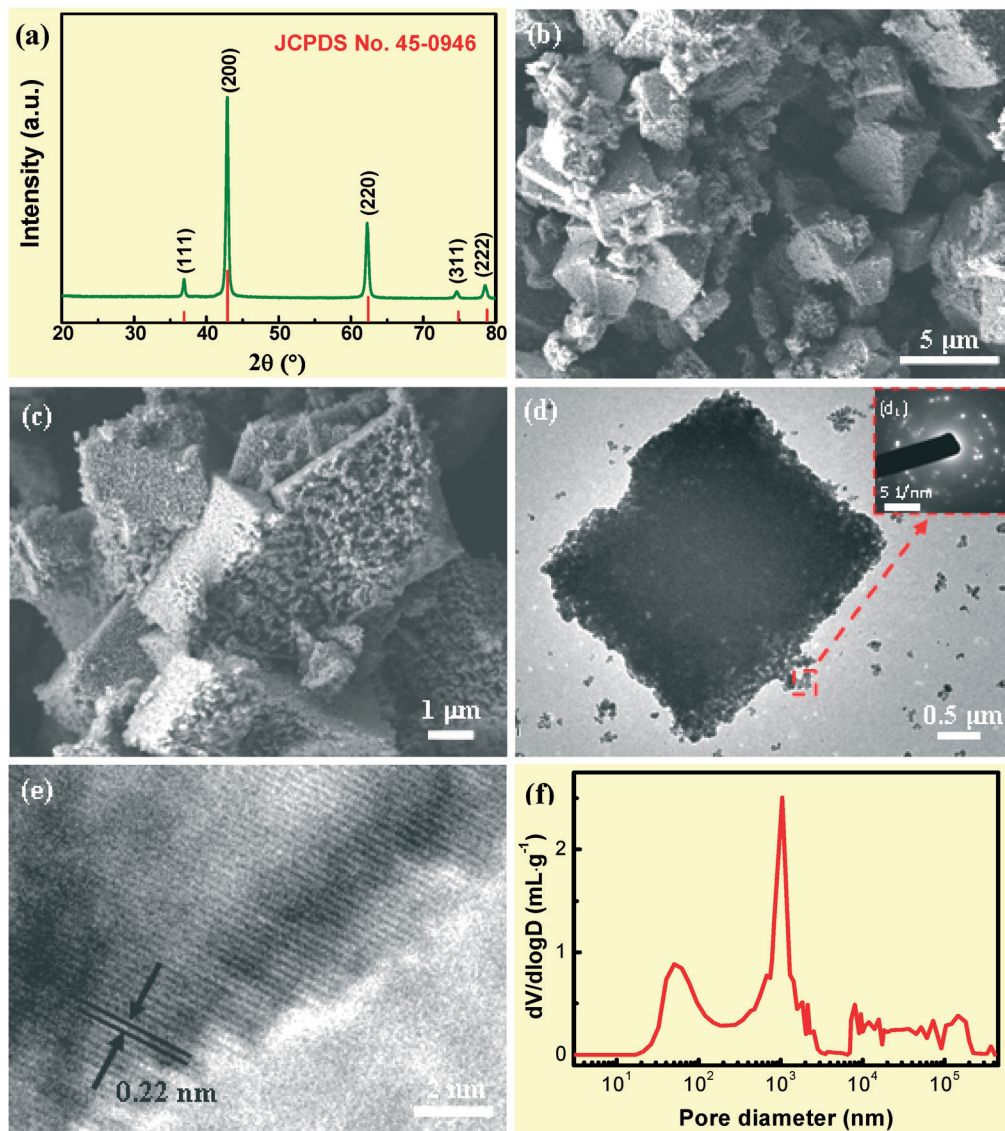


Fig. 2 (a) XRD pattern, (b, c) SEM images, (d, e) TEM images, (d<sub>1</sub>) SAED pattern and (f) pore diameter distribution of the hierarchical porous MgO superstructures calcined by the precursor at 650 °C (heating rate: 10 °C min<sup>-1</sup>) for 2.0 h, in the presence of NaCl and NP-9.

The porous structure of the product was further evaluated. As shown in Fig. S1(a) in the ESI,<sup>†</sup> the N<sub>2</sub> adsorption-desorption isotherms of the porous MgO superstructures displayed nearly type III characteristics with a slight hysteresis loop at the distinct high relative pressure of  $P/P_0 = 0.9-0.95$ , similar to the mesoporous MgO microspheres<sup>24</sup> and quite analogous to that of the porous MgO nanoplates.<sup>20</sup> The presence of the slight hysteresis loop was probably related to the minority of the micropores which exist within the porous MgO superstructures. This was further confirmed by the pore size distribution (PSD) derived from the BJH method (Fig. S1(b), ESI<sup>†</sup>), which showed that only a very few micropores (diameter < 2 nm) were detected and the majority of the pores belonged to macropores (diameter > 50 nm). Meanwhile, the multipoint BET was calculated as 23.2 m<sup>2</sup> g<sup>-1</sup>. This was smaller than that of MgO microspheres modified with ethylene glycol

(55.9 m<sup>2</sup> g<sup>-1</sup>),<sup>29</sup> and flower-like MgO (45 m<sup>2</sup> g<sup>-1</sup>)<sup>22</sup> obtained *via* an ethylene-glycol-mediated self-assembly process. However, the BET of the present porous MgO superstructures was analogous to that of flower-like MgO (24.66 m<sup>2</sup> g<sup>-1</sup>),<sup>25</sup> and much larger than that of MgO NPs (13.22 m<sup>2</sup> g<sup>-1</sup>)<sup>30</sup> prepared *via* thermal decomposition of hydroxide or MgO polyhedrons (15.9 m<sup>2</sup> g<sup>-1</sup>)<sup>31</sup> acquired by an interfacial reaction followed by calcination at 900 °C. To gain further objective information on the macropores, the porous product was further evaluated *via* mercury porosimetry. As shown in Fig. 2(f), hierarchical pores containing minor mesopores and major macropores with diameters within 20–200 nm were attributed to those existing within the body of the hierarchical porous MgO superstructures, in agreement with the SEM results (Fig. 2(c)). Pores with diameters within 300–2000 nm and even larger were ascribed to the stacking of the superstructures.

Previous work has shown that a relatively slow heating rate was favorable for the morphology preservation of  $\text{Mg}_2\text{B}_2\text{O}_5$  nanowhiskers during the calcination,<sup>32</sup> and thus, in order to investigate the effects of the calcination temperature as well as the heating rate, the precursor was calcined within 400–800 °C at a heating rate of 2 °C min<sup>-1</sup> with the other conditions kept the same. As shown in Fig. S2(a) in the ESI† the product calcined at 400 °C was composed of  $\text{MgC}_2\text{O}_4$ ,  $\text{Mg}(\text{OH})_2$ , and  $\text{MgO}$  (Fig. S2(a<sub>1</sub>), ESI†), and the existence of  $\text{Mg}(\text{OH})_2$  was probably due to the exposure of some  $\text{MgO}$  to the atmosphere of steam derived from the decomposition of  $\text{MgC}_2\text{O}_4 \cdot 2\text{H}_2\text{O}$ . When the temperature increased to 500 °C, the calcined product consisted of  $\text{Mg}(\text{OH})_2$  and  $\text{MgO}$  (Fig. S2(a<sub>2</sub>), ESI†). When the temperature was 650 °C and even higher at 800 °C, the product turned to pure phase  $\text{MgO}$  (Fig. 2(b), Fig. S2(a<sub>3</sub>, a<sub>4</sub>), ESI†). Meanwhile, when the temperature was set to 400–500 °C, the bulk  $\text{MgC}_2\text{O}_4 \cdot 2\text{H}_2\text{O}$  polyhedrons began to decompose and the profile of the precursor was destroyed to some extent (Fig. S2(b, c), ESI†). However, when the temperature went up to 650 °C, the hierarchical porous  $\text{MgO}$  superstructures tend to collapse (Fig. S2(d), ESI†), compared with those obtained at a high heating rate of 10 °C min<sup>-1</sup> (Fig. 2(c)). This showed that a lower heating rate of 2 °C min<sup>-1</sup> didn't demonstrate the expected significant effect on the morphology improvement during calcination due to the characteristics of the specific species. When the temperature was as high as 800 °C, the porous polyhedron-like superstructures disappeared completely and moreover, some larger  $\text{MgO}$  polyhedrons emerged owing to Ostwald ripening at high temperature (Fig. S2(e), ESI†). This confirmed that, to acquire hierarchical porous  $\text{MgO}$  superstructures and maintain the polyhedron-like morphology, the calcination temperature should be around 650 °C, even when calcined in the presence of  $\text{NaCl}$  and NP-9.

### 3.3 Flux and surfactant directed formation mechanism

To investigate the effect of  $\text{NaCl}$  and NP-9 on the formation of the porous  $\text{MgO}$  superstructures, the XRD patterns and SEM images of the products calcined in the presence of various additives were recorded, as shown in Fig. S3 in the ESI†. When calcined at 650 °C in the absence of any additive, the product consisted of  $\text{MgO}$  NPs and detectable minor amounts of  $\text{Mg}(\text{OH})_2$  (Fig. S3(a<sub>1</sub>), ESI†), with the polyhedron-like morphology primarily destroyed (Fig. S3(b), ESI†). The byproduct  $\text{Mg}(\text{OH})_2$  might be derived from the reaction between  $\text{MgO}$  and the water molecules retained in the porous structure. When calcined at 650 °C only in the presence of  $\text{NaCl}$ , the product turned to pure phase  $\text{MgO}$  (Fig. S3(a<sub>2</sub>), ESI†) containing multitudes of much smaller pores (Fig. S3(c), ESI†) than those formed in the previous hierarchical porous superstructures (Fig. 2), with the polyhedron-like morphology well preserved. This was very similar to the effect of  $\text{NaCl}$  on the shrinkage and even elimination of the pores during the pore-free  $\text{Mg}_2\text{B}_2\text{O}_5$  nanowhiskers formation originating from  $\text{MgBO}_2(\text{OH})$  nanowhiskers.<sup>12</sup> Meanwhile, the

TG-DTA results recorded during the thermal decomposition of  $\text{MgC}_2\text{O}_4 \cdot 2\text{H}_2\text{O}$  in the presence of  $\text{NaCl}$  (Fig. S3(c<sub>1</sub>), ESI†) showed a similar variation tendency to that displayed for the decomposition of the pure phase of  $\text{MgC}_2\text{O}_4 \cdot 2\text{H}_2\text{O}$  (Fig. 1(d)). Taking the existence of  $\text{NaCl}$  into consideration, the mass variation *vs.* temperature reconfirmed the decomposition of  $\text{MgC}_2\text{O}_4 \cdot 2\text{H}_2\text{O}$  *via* eqn (4) and (5).

In contrast, when calcined only in the presence of NP-9, the product was composed of  $\text{MgO}$  NPs and significant amounts of  $\text{Mg}(\text{OH})_2$  (Fig. S3(a<sub>3</sub>), ESI†) with the polyhedron-like morphology largely changed into an agglomeration (Fig. S3(d), ESI†). As a dispersing agent,<sup>33</sup> NP-9 consisted of a hydrophobic nonyl side chain and hydrophilic ethoxy chain,<sup>34</sup> and the hydrophilic chain might be adsorbed onto the surfaces of the precursors, forming a precursor@ethoxy core-shell structure. The ethoxy shell prevented the evaporation of the water derived from the dehydration of the precursor  $\text{MgC}_2\text{O}_4 \cdot 2\text{H}_2\text{O}$ , leading to the formation of significant amounts of the byproduct  $\text{Mg}(\text{OH})_2$  (Fig. S3(a<sub>3</sub>), ESI†) in turn during the subsequent decomposition of  $\text{MgC}_2\text{O}_4$  into  $\text{MgO}$  (eqn (5)). Taking the calcination of the precursor in the presence of both  $\text{NaCl}$  and NP-9 at the same temperature into account, the product was pure phase  $\text{MgO}$  without any  $\text{Mg}(\text{OH})_2$  detected (Fig. 2(a, c)). This was probably due to the existence of  $\text{NaCl}$ , which enhanced the transportation of water and thus interrupted the side reaction between the  $\text{MgO}$  product and water. When the temperature was increased up to 800 °C, the final product calcined in the absence of any additives was proved to be pure phase  $\text{MgO}$  NPs (Fig. S3(a<sub>4</sub>, e), ESI†), although with the polyhedron-like morphology almost completely destroyed on the one hand and much smaller diameters as well as lower crystallinity on the other hand, in comparison to the previous results (Fig. S2(a<sub>4</sub>, e), ESI†).

In addition, the thermal decomposition phenomena of NP-9 with or without the precursor was also observed so as to obtain a deeper insight into the effect of NP-9. During the heating of the precursor (heating rate: 10 °C min<sup>-1</sup>) in the presence of NP-9 and  $\text{NaCl}$ , vapour was found at *ca.* 200 °C, white smog appeared at *ca.* 400 °C with a yellow liquid condensed on the inner wall of the quartz tube ends out of the furnace, and black powders were obtained at *ca.* 650 °C with much more yellow liquid condensed inside both ends of the tube. After cooling, a light brown powder was acquired. Comparatively, when NP-9 was put into the porcelain boat for calcination with the same heating rate, carbon black was observed at 650 °C which, however, disappeared once the boat was kept isothermal for some time. As a matter of fact, when the heating rate was decreased to 2 °C min<sup>-1</sup>, vapour appeared at similar *ca.* 200 °C, heavy white smog was observed at 300 °C, and only a little carbon black was left at 400 °C which was found to disappear when the boat was kept isothermal at 500 °C for 1.5 h.

Based on the above experimental results as well as the thermal decomposition phenomena of NP-9 in the presence or absence of the precursor, the probable  $\text{NaCl}$  and NP-9

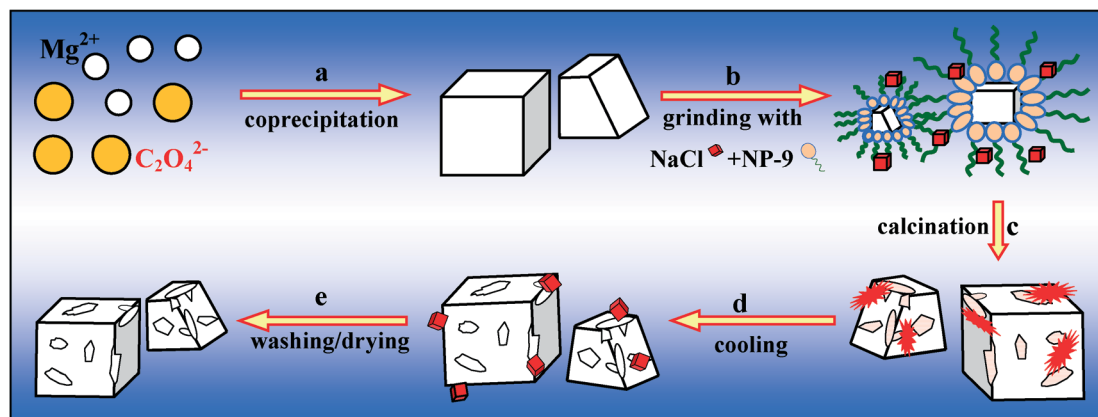


**Fig. 3** Flux and surfactant directed formation of hierarchical porous MgO superstructures. (a) Room temperature coprecipitation of  $\text{MgCl}_2$  and  $\text{Na}_2\text{C}_2\text{O}_4$  solutions and subsequent Ostwald ripening during aging led to high crystallinity well-faceted  $\text{MgC}_2\text{O}_4 \cdot 2\text{H}_2\text{O}$  micron polyhedrons; (b) grinding the polyhedrons with the flux  $\text{NaCl}$  and surfactant NP-9 resulted in a slurry containing  $\text{NaCl}$  particles and a NP-9 wrapped precursor; (c) heating of the precursor slurry up to  $650\text{ }^\circ\text{C}$  produced porous MgO mingled with significant carbon black due to the decomposition and further carbonization of NP-9, and during the isothermal period, the carbon black disappeared and the gradually formed  $\text{NaCl}$  vapour favored the reasonable shrinkage of the pores and further morphology preservation; (d) during cooling,  $\text{NaCl}$  recrystallized, leading to porous MgO polyhedrons at the same time; (e) final washing and drying gave rise to the hierarchical porous MgO superstructures with the polyhedron-like morphology largely preserved.

assisted formation mechanism of the hierarchical porous MgO superstructures could thus be figured out, as shown in Fig. 3. Room temperature coprecipitation of  $\text{MgCl}_2$  and  $\text{Na}_2\text{C}_2\text{O}_4$  solutions first led to relatively low crystallinity micron polyhedrons of  $\text{MgC}_2\text{O}_4 \cdot 2\text{H}_2\text{O}$  with small NPs attached on the surfaces. Then, high crystallinity well-faceted  $\text{MgC}_2\text{O}_4 \cdot 2\text{H}_2\text{O}$  micron polyhedrons were obtained *via* washing and drying owing to Ostwald ripening during the aging after coprecipitation (Fig. 3(a)). The precursor was ground with the flux  $\text{NaCl}$  and surfactant NP-9 for 0.5 h, resulting in a slurry containing  $\text{NaCl}$  particles and a NP-9 capped precursor, which was then transferred into the porcelain boat for calcination (Fig. 3(b)). When the temperature went up continuously, the precursor dehydrated at *ca.*  $200\text{ }^\circ\text{C}$  first, bringing about the surfactant capped porous polyhedrons. When the temperature increased up to  $650\text{ }^\circ\text{C}$ , the original precursor further decomposed and released  $\text{CO}$  as well as  $\text{CO}_2$  gas, producing hierarchical porous MgO powder which, however, was mingled with significant carbon black due to the decomposition and further carbonization of NP-9. At the subsequent isothermal state, the carbon black gradually changed into  $\text{CO}_2$  and meanwhile, the flux  $\text{NaCl}$  gradually melted to some extent and formed  $\text{NaCl}$  vapour (Fig. 3(c)).<sup>35</sup> In other words, the evaporated  $\text{NaCl}$  could act as a gaseous flux, giving rise to the reasonable shrinkage of the pores as well as the improvement of the crystallinity or strength of the pore walls within the porous MgO superstructures. Apparently, the gaseous  $\text{NaCl}$  flux was extremely important for the formation of the porous structures.  $\text{NaCl}$  recrystallized out of the porous MgO in the course of cooling (Fig. 3(d)), and the hierarchical porous MgO superstructures with a well-preserved polyhedron-like profile were finally obtained *via* a washing and drying post-treatment (Fig. 3(e)). This was analogous to the  $\text{NaCl}$  (g) aided molten salt growth of ternary oxide nanorods

below the melting point of  $\text{NaCl}$ ,<sup>35</sup> and was also confirmed by the  $\text{NaCl}$  assisted formation of pore-free  $\text{Mg}_2\text{B}_2\text{O}_5$  nanowhiskers *via* the thermal conversion of  $\text{MgBO}_2(\text{OH})$  nanowhiskers at  $650\text{--}700\text{ }^\circ\text{C}$ .<sup>36</sup>

Reasonably, NP-9 and  $\text{NaCl}$  played key roles in the formation of the hierarchical porous MgO superstructures. Dehydration of the oxalate precursor and release of  $\text{CO}$  as well as  $\text{CO}_2$  gas brought about the pores among the MgO NPs. As a nonionic surfactant, NP-9 served as the dispersing agent and thus prevented the porous MgO particles from aggregating with each other. The gradually formed  $\text{NaCl}$  vapor at  $650\text{ }^\circ\text{C}$  could migrate through the porous structure, favoring the *in situ* crystallization of MgO after the completion of the phase conversion from the oxalate precursor, strengthen the toughness of the backbone and further realize the preservation of the precursor's original polyhedron-like morphology. Obviously, it was the successive and synergistic effect of NP-9 and  $\text{NaCl}$  that promoted the final formation of the present hierarchical porous MgO superstructures.

### 3.4 Hierarchical porous MgO superstructures as the adsorbents for MB

As described above, porous MgO superstructures with high crystallinity and a well faceted profile have been obtained *via* the novel facile thermal conversion synthesis. However, as known, poor crystallinity and hydrothermal stability has emerged as a big challenge in the real applications of porous structures. Since the as-prepared hierarchical porous MgO superstructures contained plenty of macropores and mesopores within the body (Fig. 2(f)), in addition to the main purpose or, in other words, the target of our work, the as-synthesized porous MgO superstructures were preliminarily evaluated as adsorbents for the traditional removal of MB.

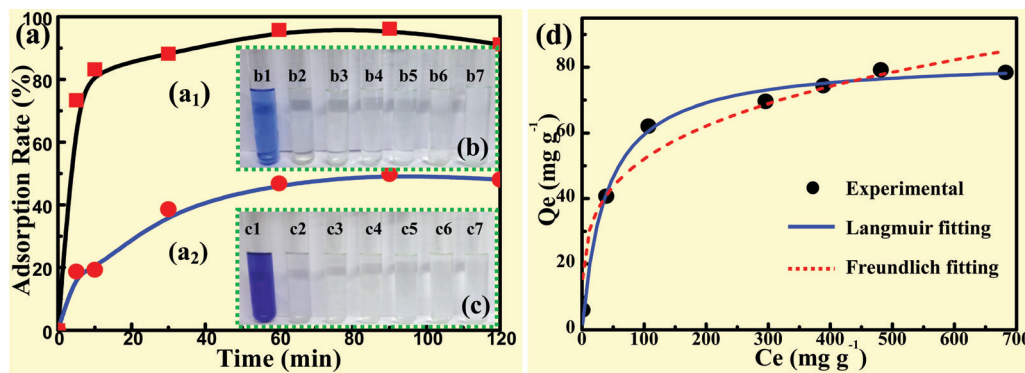


Fig. 4 Variation of (a) adsorption rate and (b, c) color for mimetic solutions containing different concentrations of methylene blue vs. adsorption time, as well as (d) adsorption isotherms fitted according to the Langmuir and Freundlich models, with 30 mg of the hierarchical porous MgO superstructures as adsorbents for 20 mL of different concentrations of methylene blue containing solutions. Concentration ( $\text{mg L}^{-1}$ ): (a<sub>1</sub>)-10, (a<sub>2</sub>)-100.

For a mimetic solution containing a relatively low concentration of MB ( $10 \text{ mg L}^{-1}$ ), the adsorption rate rapidly increased to 73.4% at 5 min, reached 83.2% at 10 min, and then vibrated with a highest value of 95.78% at 60 min (Fig. 4(a<sub>1</sub>)). This was somewhat lower than 98% of adsorbents for Cu-MSM-3<sup>37</sup> due to the present relatively small specific surface area, but higher than 90% for  $\text{Co}_{0.85}\text{Se}$  nanostructures<sup>38</sup> and 66% for porous  $\text{Mg}_5(\text{CO}_3)_4(\text{OH})_2 \cdot 4\text{H}_2\text{O}$  nanorods,<sup>39</sup> higher than 85% for  $\text{TiO}_2$  (P25)-graphene nanocomposites under UV light irradiation,<sup>40</sup> and also much better than the maximum of 65.9% for mesoporous  $\text{WO}_3$  even in photocatalytic conditions.<sup>41</sup> Meanwhile, the light blue solution faded away and became transparent and colorless immediately after 5 min (Fig. 4(b)). In contrast however, for a solution containing a higher concentration of MB ( $100 \text{ mg L}^{-1}$ ), the adsorption rate was 19.3% at 10 min, 38.6% at 30 min, 46.8% at 60 min, and vibrated thereafter with a climax value of 49.8% at 90 min (Fig. 4(a<sub>2</sub>)). Simultaneously, the heavy blue solution also faded away quickly, without the distinct gradual colour change (Fig. 4(c)).

The variation of the equilibrium adsorption capacities ( $q_e$ ) vs. equilibrium concentration ( $c_e$ ) was plotted in Fig. 4(d). As shown,  $q_e$  gradually increased with the increase in  $c_e$ . The adsorption isotherms of the hierarchical porous MgO superstructures used for the MB solutions were fitted according to the traditional Langmuir and Freundlich models, indicated by the blue solid line and red dotted line, respectively. The corresponding isotherm parameters were listed in Table 1. As

shown, the regression coefficient ( $R^2$ ) via Langmuir model was 0.991, much higher than that of the Freundlich model (0.958). This revealed that the adsorption of MB on the as-synthesized hierarchical porous MgO superstructures more likely conformed to the Langmuir adsorption rather than the Freundlich adsorption. In other words, the adsorption of MB on the present porous MgO superstructures was a monolayer adsorption process, which was generally characteristic of the chemisorption process.<sup>42</sup> In addition, via the Langmuir model, the maximum adsorption capacity ( $q_m$ ) was calculated as  $82.703 \text{ mg g}^{-1}$ . This was somewhat lower than that of commercial activated carbon,<sup>43</sup> similar to that of fibrous clay minerals<sup>44</sup> and pyrolysed furniture<sup>45</sup> but nevertheless much higher than that of Coconut husk based activated carbon,<sup>46</sup> charcoal,<sup>47</sup> and some other agricultural as well as industrial solid wastes.<sup>48</sup>

### 3.5 Hierarchical porous MgO superstructures as the catalyst supports for SWCNTs growth

Nanostructured MgO are widely employed as catalyst supports to load metal NPs for CVD growth of CNTs and graphene,<sup>49,50</sup> as well as methane coupled oxidation.<sup>51</sup> The hierarchical porous MgO can serve as a support to anchor the ultra-fine metal NPs for the catalytic decomposition of methane for CNT deposition. SWCNTs have been accepted as the high end of CNT technology because of their excellent intrinsic properties, such as high specific surface area, low defect density, and tunable electronic characteristics according to their chirality. Herein, the oxalate derived hierarchical MgO superstructures were thus employed as porous supports to load Fe NPs for SWCNTs growth. As shown in Fig. 5, high quality SWCNTs were grown out. Due to the strong van der Waals interactions, the as-obtained CNTs prefer to form bundles. A high yield of ca. 7% was achieved, which was attributed to the fact that the SWCNTs were facile for extending out of the interconnected pores of the MgO support. The SWCNTs had a diameter of 0.8–2.5 nm, which was confirmed by the high resolution TEM image (Fig. 5(b))

Table 1 Corresponding parameters of the Langmuir and Freundlich isotherms for the adsorption of methylene blue

Isotherm	Equation	Parameter	Constants
Langmuir model	$q_e = \frac{q_m K_L C_e}{1 + K_L C_e}$	$R^2$	0.991
		$q_m (\text{mg g}^{-1})$	82.703
		$K_L (\text{L mg}^{-1})$	0.026
Freundlich model	$q_e = K_F C_e^n$	$R^2$	0.948
		$n$	3.925
		$K_F$	16.114

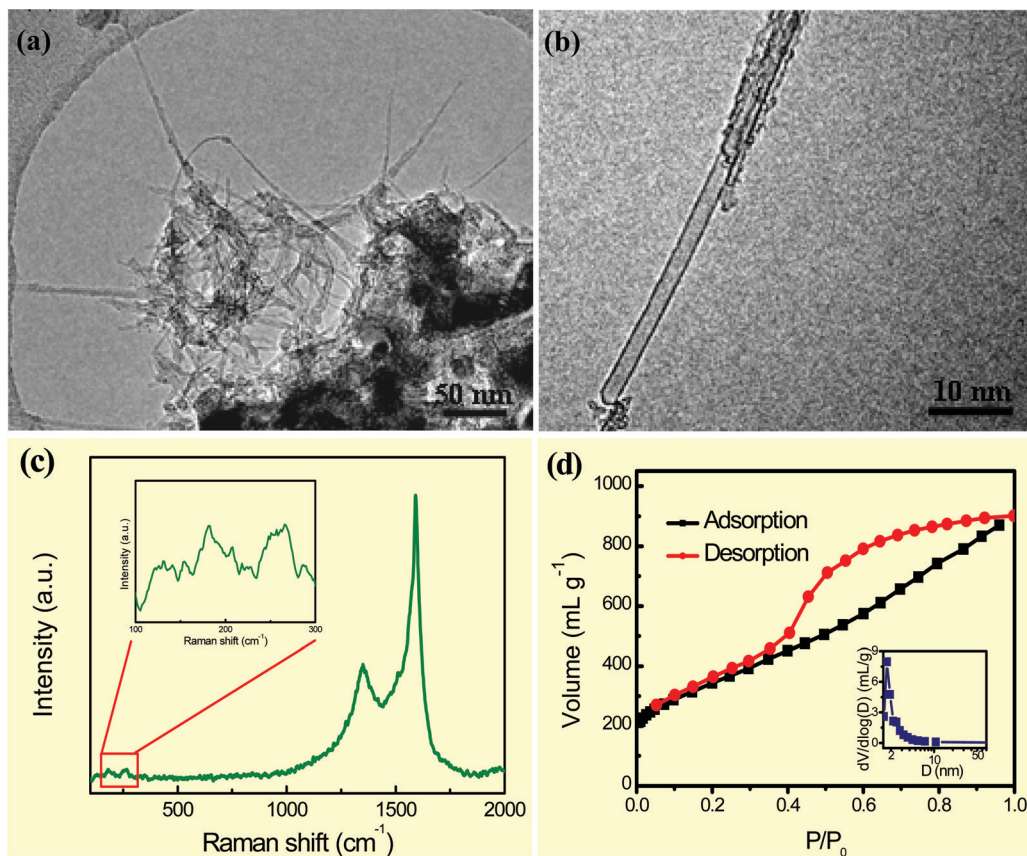


Fig. 5 (a) TEM, (b) high resolution TEM images, (c) Raman spectrum (inset RBM peaks), and (d)  $N_2$  adsorption–desorption isotherms (inset pore size distribution) of the SWCNTs grown on the hierarchical porous MgO superstructures supported iron catalysts.

and radial breathing modes shown in the Raman spectrum (Fig. 5(c)). A quite high  $I_G/I_D$  ratio of 3.9 was available, which was competitive to the SWCNTs grown on the Fe/Mg/Al layered double hydroxide derived catalyst (*ca.* 4.0)<sup>52</sup> and higher than the routine MgO powder derived catalyst (2.0–3.5).<sup>53</sup> The MgO support can be facilely removed by HCl washing, and SWCNTs with a very high purity of >98 wt% were available.

As shown in Fig. 5(d), the  $N_2$  adsorption–desorption isotherms of the purified SWCNTs exhibited a typical type IV isotherm with apparent H4 hysteresis loop. The pore size distribution (inset of Fig. 5(d)) illustrated that micropores with diameters < 2 nm contributed the majority to the pore volume. The as-obtained SWCNTs afforded a BET specific surface area, total pore volume, and average pore size of  $1232 \text{ m}^2 \text{ g}^{-1}$ ,  $1.23 \text{ cm}^3 \text{ g}^{-1}$ , and 1.7 nm, respectively. The specific surface area was much higher than that of other SWCNTs obtained by CVD growth on a layered double hydroxide derived catalyst ( $500\text{--}1100 \text{ m}^2 \text{ g}^{-1}$ ),<sup>52</sup> high-pressure CO conversion ( $400\text{--}700 \text{ m}^2 \text{ g}^{-1}$ ),<sup>54</sup> and arc-discharge method ( $100\text{--}500 \text{ m}^2 \text{ g}^{-1}$ ).<sup>55</sup> This is ascribed to the uniform distribution of the Fe catalysts on the 3D hierarchical porous MgO support, which benefits their high temperature stability as well as the resultant CVD growth of the SWCNTs within limited space resistance. Such 3D

hierarchical porous MgO is very efficient for the catalytic growth of high end nanomaterials, such as CNTs. It is also expected to serve as a template for 3D graphene and SWCNT/graphene hybrid deposition.

## 4. Conclusions

3D hierarchical porous MgO superstructures with a well faceted profile and high crystallinity were fabricated *via* a facile room temperature coprecipitation of  $\text{Na}_2\text{C}_2\text{O}_4$  and  $\text{MgCl}_2 \cdot 6\text{H}_2\text{O}$  solutions followed by a mild flux NaCl and surfactant NP-9 directed thermal conversion of the resultant precursor at  $650 \text{ }^\circ\text{C}$ . The successive and synergistic effect of NaCl and NP-9 promoted the final formation of the hierarchical porous MgO superstructures. NP-9 served as a dispersing agent and restrained the porous MgO particles from aggregating with each other, whereas NaCl favored the *in situ* crystallization of porous MgO, enhanced the toughness of the backbone and further realized the polyhedron-like morphology preservation. The as-obtained porous MgO superstructures were preliminarily evaluated as adsorbents for the removal of MB as well as a catalyst carrier for SWCNTs growth, aiming to present a relatively whole outlook for our research. The excellent adsorption capacity for MB, as well as effective catalyst support for SWCNT growth revealed the

as-obtained hierarchical porous MgO superstructures are great potential candidates in related fields such as environmental protection, heterogeneous catalysis, as well as nanomaterials production.

## Acknowledgements

This work was supported by the National Natural Science Foundation of China (No. 21276141), the State Key Laboratory of Chemical Engineering, China (No. SKL-ChE-12A05), the Project of Shandong Province Higher Educational Science and Technology Program, China (J10LB15), and the Excellent Middle-Aged and Young Scientist Award Foundation of Shandong Province, China (BS2010CL024). The authors thank Dr. Mingbo Yue at the School of Chemistry and Chemical Engineering, Qufu Normal University for their helpful discussion, and also are obliged to the reviewers for their constructive suggestions.

## References

- H. Colfen and M. Antonietti, *Angew. Chem. Int. Ed.*, 2005, **44**, 5576–5591.
- Y. Li, Z.-Y. Fu and B.-L. Su, *Adv. Funct. Mater.*, 2012, **22**, 4634–4667.
- M.-Q. Zhao, Q. Zhang, X.-L. Jia, J.-Q. Huang, Y.-H. Zhang and F. Wei, *Adv. Funct. Mater.*, 2010, **20**, 677–685.
- Q. Zhang, J. Q. Huang, M. Q. Zhao, W. Z. Qian and F. Wei, *ChemSusChem*, 2011, **4**, 864–889.
- J. Tantirungrotechai, S. Thepwater and B. Yoosuk, *Fuel*, 2013, **106**, 279–284.
- K. Karthikeyan, S. Amaresh, V. Aravindan and Y. S. Lee, *J. Mater. Chem. A*, 2013, **1**, 4105–4111.
- Z. Cui, G. W. Meng, W. D. Huang, G. Z. Wang and L. D. Zhang, *Mater. Res. Bull.*, 2000, **35**, 1653–1659.
- Q. Yang, J. Sha, L. Wang, J. Wang and D. R. Yang, *Mater. Sci. Eng. C*, 2006, **26**, 1097–1101.
- P. Yan, C. H. Ye, X. S. Fang, J. W. Zhao, Z. Y. Wang and L. D. Zhang, *Chem. Lett.*, 2005, **34**, 384–385.
- Y. F. Hao, G. W. Meng, C. H. Ye, X. R. Zhang and L. D. Zhang, *J. Phys. Chem. B*, 2005, **109**, 11204–11208.
- Y. G. Yan, L. X. Zhou and Y. Zhang, *J. Phys. Chem. C*, 2008, **112**, 19831–19835.
- W. C. Zhu, Q. Zhang, L. Xiang, F. Wei, X. T. Sun, X. L. Piao and S. L. Zhu, *Cryst. Growth Des.*, 2008, **8**, 2938–2945.
- P. Tian, J. W. Ye, N. Xu, W. T. Gong, Q. S. Zhang, Y. Lin and G. L. Ning, *Chem. Commun.*, 2011, **47**, 12008–12010.
- W. Z. Wang, C. K. Xu, G. H. Wang, Y. K. Liu and C. L. Zheng, *Adv. Mater.*, 2002, **14**, 837–840.
- M. Y. Li, W. S. Dong, C. L. Liu, Z. Liu and F. Q. Lin, *J. Cryst. Growth*, 2008, **310**, 4628–4634.
- L. Yan, J. Zhuang, X. M. Sun, Z. X. Deng and Y. D. Li, *Mater. Chem. Phys.*, 2002, **76**, 119–122.
- N. Sutradhar, A. Sinhamahapatra, B. Roy, H. C. Bajaj, I. Mukhopadhyay and A. B. Panda, *Mater. Res. Bull.*, 2011, **46**, 2163–2167.
- Y. Jia, T. Luo, X. Y. Yu, B. Sun, J. H. Liu and X. J. Huang, *RSC Adv.*, 2013, **3**, 5430–5437.
- J. C. Yu, A. W. Xu, L. Z. Zhang, R. Q. Song and L. Wu, *J. Phys. Chem. B*, 2004, **108**, 64–70.
- H. X. Niu, Q. Yang, K. B. Tang and Y. Xie, *Microporous Mesoporous Mater.*, 2006, **96**, 428–433.
- M. Sharma and P. Jeevanandam, *J. Alloys Compd.*, 2011, **509**, 7881–7885.
- S. W. Bain, Z. Ma, Z. M. Cui, L. S. Zhang, F. Niu and W. G. Song, *J. Phys. Chem. C*, 2008, **112**, 11340–11344.
- N. Sutradhar, A. Sinhamahapatra, S. K. Pahari, P. Pal, H. C. Bajaj, I. Mukhopadhyay and A. B. Panda, *J. Phys. Chem. C*, 2011, **115**, 12308–12316.
- J. B. Zhou, S. L. Yang and J. G. Yu, *Colloids Surf. A*, 2011, **379**, 102–108.
- X. Y. Yu, T. Luo, Y. Jia, Y. X. Zhang, J. H. Liu and X. J. Huang, *J. Phys. Chem. C*, 2011, **115**, 22242–22250.
- C. Y. Cao, J. Qu, F. Wei, H. Liu and W. G. Song, *ACS Appl. Mater. Interfaces*, 2012, **4**, 4283–4287.
- W. C. Zhu, Z. Z. Liang, X. F. Liu, H. Zhang, Y. J. Zheng, X. L. Piao and Q. Zhang, *Powder Technol.*, 2012, **226**, 165–172.
- L. H. Ai, H. T. Yue and J. Jiang, *Nanoscale*, 2012, **4**, 5401–5408.
- J. Jin, Z. P. Zhang, H. L. Ma, X. B. Lu, J. P. Chen, Q. Zhang, H. J. Zhang and Y. W. Ni, *Mater. Lett.*, 2009, **63**, 1514–1516.
- Z. Camtakan, S. A. Erenturk and S. D. Yusan, *Environ. Prog. Sustainable Energy*, 2012, **31**, 536–543.
- Y. He, *Mater. Lett.*, 2006, **60**, 3511–3513.
- W. Zhu, L. Xiang, Q. Zhang, X. Zhang, L. Hu and S. Zhu, *J. Cryst. Growth*, 2008, **310**, 4262–4267.
- Z. Y. Cai, X. R. Xing, R. B. Yu and X. Y. Sun, *Inorg. Chem.*, 2007, **46**, 7423–7427.
- F. Yang, G. Li, R. Liu, B. Zhang, Y. Liu and Z. X. Wang, *Acta Chim. Sin.*, 2009, **67**, 723–728.
- P. M. Rorvik, T. Lyngdal, R. Saeterli, A. T. J. van Helvoort, R. Holmestad, T. Grande and M. A. Einarsrud, *Inorg. Chem.*, 2008, **47**, 3173–3181.
- W. C. Zhu, Q. Zhang, L. Xiang and S. L. Zhu, *Cryst. Growth Des.*, 2011, **11**, 709–718.
- Y. Cao, H. Zou, H. Wei, Y. Wen and Y. Wang, *Chin. J. Inorg. Chem.*, 2012, **28**, 1705–1711.
- J.-F. Zhao, J.-M. Song, C.-C. Liu, B.-H. Liu, H.-L. Niu, C.-J. Mao, S.-Y. Zhang, Y.-H. Shen and Z.-P. Zhang, *CrystEngComm*, 2011, **13**, 5681–5684.
- L. Song and S. Zhang, *Colloids Surf. A*, 2009, **350**, 22–25.
- H. Zhang, X. J. Lv, Y. M. Li, Y. Wang and J. H. Li, *ACS Nano*, 2010, **4**, 380–386.
- B. X. Liu, J. S. Wang, H. Y. Li, J. S. Wu and Z. F. Li, *Chin. J. Inorg. Chem.*, 2012, **28**, 465–470.
- X. H. Song, Y. B. Wang, K. A. Wang and R. Xu, *Ind. Eng. Chem. Res.*, 2012, **51**, 13438–13444.
- B. Bestani, N. Benderdouche, B. Benstaali, M. Belhakem and A. Addou, *Bioresour. Technol.*, 2008, **99**, 8441–8444.
- M. Hajjaji, A. Alami and A. El Bouadili, *J. Hazard. Mater.*, 2006, **135**, 188–192.
- C. I. Sainz-Diaz and A. J. Griffiths, *Fuel*, 2000, **79**, 1863–1871.

- 46 H. Tamai, T. Kakii, Y. Hirota, T. Kumamoto and H. Yasuda, *Chem. Mater.*, 1996, **8**, 454–462.
- 47 F. Banat, S. Al-Asheh, R. Al-Ahmad and F. Bni-Khalid, *Bioresour. Technol.*, 2007, **98**, 3017–3025.
- 48 M. Rafatullah, O. Sulaiman, R. Hashim and A. Ahmad, *J. Hazard. Mater.*, 2010, **177**, 70–80.
- 49 X. Zhu, G. Ning, Z. Fan, J. Gao, C. Xu, W. Qian and F. Wei, *Carbon*, 2012, **50**, 2764–2771.
- 50 Q. Zhang, J.-Q. Huang, W.-Z. Qian, Y.-Y. Zhang and F. Wei, *Small*, 2013, **9**, 1237–1265.
- 51 U. Zavyalova, M. Geske, R. Horn, G. Weinberg, W. Frandsen, M. Schuster and R. Schlogl, *ChemCatChem*, 2011, **3**, 949–959.
- 52 M. Q. Zhao, Q. Zhang, J. Q. Huang, J. Q. Nie and F. Wei, *Carbon*, 2010, **48**, 3260–3270.
- 53 H. Yu, Q. Zhang, Q. F. Zhang, Q. X. Wang, G. Q. Ning, G. H. Luo and F. Wei, *Carbon*, 2006, **44**, 1706–1712.
- 54 C. M. Yang, K. Kaneko, M. Yudasaka and S. Iijima, *Nano Lett.*, 2002, **2**, 385–388.
- 55 L. A. Montoro and J. M. Rosolen, *Carbon*, 2006, **44**, 3293–3301.